Development of Cellular Magnetic Dipoles in Magnetotactic Bacteria

Damien Faivre,[†] Anna Fischer,[†] Inés Garcia-Rubio,[‡] Giovanni Mastrogiacomo,[§] and Andreas U. Gehring[§*]
[†]Department of Biomaterials, Max Planck Institute of Colloids and Interfaces, Potsdam, Germany; and [‡]Laboratory of Physical Chemistry and [§]Institute of Geophysics, ETH Zurich, Zurich, Switzerland

ABSTRACT Magnetotactic bacteria benefit from their ability to form cellular magnetic dipoles by assembling stable single-domain ferromagnetic particles in chains as a means to navigate along Earth's magnetic field lines on their way to favorable habitats. We studied the assembly of nanosized membrane-encapsulated magnetite particles (magnetosomes) by ferromagnetic resonance spectroscopy using *Magnetospirillum gryphiswaldense* cultured in a time-resolved experimental setting. The spectroscopic data show that 1), magnetic particle growth is not synchronized; 2), the increase in particle numbers is insufficient to build up cellular magnetic dipoles; and 3), dipoles of assembled magnetosome blocks occur when the first magnetite particles reach a stable single-domain state. These stable single-domain particles can act as magnetic docks to stabilize the remaining and/or newly nucleated superparamagnetic particles in their adjacencies. We postulate that docking is a key mechanism for building the functional cellular magnetic dipole, which in turn is required for magnetotaxis in bacteria.

INTRODUCTION

All magnetotactic bacteria (MTB) have in common the biomineralization of membrane-encapsulated nanosized ferrimagnetic particles (magnetosomes) with narrow size and shape distributions (1,2). The assembly of mature magnetosomes into chains results in intracellular single magnetic dipoles that are usually large enough to interact with the Earth's magnetic field and operate as a compass to navigate MTB toward favorable habitats (3–5). The biomineralization of magnetosomes and their route to functionality have not yet been resolved. Genetic studies demonstrate that the chain arrangements of magnetosomes along cytoskeletal filaments in the MTB of *Magnetospirilla* strains are controlled by the MamJ and MamK proteins (6,7). In *M. gryphiswaldense* (the MTB used in this study), magnetite nucleates in discrete vesicles, and then the growing magnetosomes move like beads along the cytoskeletal filament to form a tight chain (7). Moreover, it has been reported that the MamGFDC proteins or FtsZ-like protein can regulate the size of the magnetite (Fe_3O_4) crystals in *M. gryphiswaldense* (8,9). Although numerous genetic and proteomic studies have examined the processes that lead to functional cellular magnetic dipoles, there have been only limited and inconclusive studies on the magnetic evolution that occurs during the assembly of magnetosome chains (10,11). Such information would not only complement studies of the biological mechanism underlying chain formation, it would also provide insight into the design of functional cellular magnetic dipoles as key factors in magnetotaxis.

During the biomineralization of magnetite in MTB, particles of variable size are formed (8,9,12). From a magnetic perspective, small particles (<30 nm) at room temperature are generally in a superparamagnetic (SPM) state, in which their magnetic moments point in random directions due to thermal fluctuation (13). The stable single domain (SSD) state can be achieved by interactions between the particles and/or growth to a specific blocking size (14,15). To unravel the interplay between growth and interaction of magnetite particles during the formation of cellular dipoles in MTB, we studied the magnetic traits of the strain *M. gryphiswaldense* during iron-induced, time-resolved chain formation (16). The magnetic properties were analyzed by ferromagnetic resonance (FMR) spectroscopy. Recent FMR studies provided compelling evidence that this method makes it possible to detect anisotropy of aligned mature magnetosomes in MTB as well as the coupling fields within the chains (17–20). In this study we combined FMR spectroscopy with transmission electron microscopy (TEM) and optical density measurements to obtain semiquantitative measures of magnetosome concentration (21). Both of these techniques provide nonmagnetic information about the growth of magnetosomes with time. Based on the experimental results, we propose a mechanism by which the magnetic state of the magnetosomes facilitates their assembly.

MATERIALS AND METHODS

Time-resolved growth and nonmagnetic analysis of magnetosome assembly

The *M. gryphiswaldense* strain MSR-1 (DSM 6361) was grown as described by Faivre et al. (16) using aerobe conditions for the low-iron medium. To start magnetite production, the cells were transferred into a micro-aerobic, low-carbon medium (in which no cell division occurs) followed by the addition of 30 μM ferric citrate. At given time intervals,

Submitted March 3, 2010, and accepted for publication May 21, 2010.

*Correspondence: andreas.gehring@erdw.ethz.ch

Anna Fischer's present address is Institute of Chemistry, Berlin, Germany.

Giovanni Mastrogiacomo's present address is Swiss Steel, Emmenbrücke, Switzerland.

Editor: Michael Edidin.

0006-3495/10/08/1268/6 $2.00

doi: 10.1016/j.bpj.2010.05.034

12 mL samples were taken from the culture. In a 1 mL sample, the semi-quantitative magnetosome content was determined by light scattering (λ = 565 nm; Shimadzu UV mini 1240 spectrophotometer) in parallel and perpendicular magnetic fields of 0.2 T. The relative ratio of the scattering intensities (C_{mag}) was used to monitor the magnetosome production (21). The remaining fraction was promptly centrifuged (4°C) and repeatedly washed with water before it was quenched with a 1% formaldehyde solution (0.1% vol/vol). The quenched cells were washed with water before grid preparation for TEM (one drop) and freeze-dried for FMR analysis (11 mL). Transmission electron micrographs were acquired with a Zeiss EM Omega 912X at an acceleration voltage of 120 kV. Particle dimensions were analyzed using standard analytical software for processing digitized electron microscope images (ImageJ). To determine the size distribution, 900 particles in ~30 cells were counted.

Basics of FMR and the diagnostic spectral parameters

FMR spectroscopy is a special application of the classical electron spin resonance (ESR) spectroscopy approach, whereby the absorption of microwave energy by molecules, ions, or atoms possessing electrons with unpaired spins is measured as a function of an applied field (22). Absorption occurs when the following resonance condition is fulfilled:

$$h\nu = g\,\mu_B\,B, \tag{1}$$

where h = Planck's constant, ν = microwave frequency, g = splitting factor, μ_B = Bohr magneton, and B is the magnetic field. In contrast to ESR spectroscopy, FMR spectroscopy detects coupled spins of a magnetically ordered phase, and therefore the applied field that leads to resonance conditions is affected by the internal magnetic field of the sample. In FMR experiments, the applied static field excites the precession of the total magnetic moment around a local field. Relaxation processes damp the precession and the magnetization aligns with the local field. If the irradiation frequency (typically between 1 and 35 GHz: S-band 2–4 GHz and X-band 8–12 GHz) perpendicular to the applied field coincides with the precessional frequency, the resonance condition is fulfilled and microwave power is absorbed by the sample (23). The resonance condition can be rewritten as

$$h\nu = g_{eff}\,\mu_B\,B_{app}, \tag{2}$$

where g_{eff} is the effective splitting factor and B_{app} is the applied field. The g_{eff} in Eq. 2 takes into account the effect of the internal field B_{int} that cannot be measured directly. This field contains different contributions that include the demagnetization field, the exchange field, and the magnetocrystalline and magnetostrictive energies. The diagnostic parameters g_{eff}, B_{res}, ΔB, and A are often used to describe the FMR spectra obtained from MTB (17,19,24). The effective splitting factor g_{eff} can be calculated from Eq. 2, whereby the variable ν is given by the spectrometer used, and B_{app}, considered as the resonance field B_{res}, is the field at maximum absorption determined by the zero-crossing in the derivative spectrum (Fig. 1). The linewidth ΔB is defined as the full width at half-maximum of the absorption spectrum (Fig. 1). In the literature, ΔB is often considered as the sum of two contributions (25):

$$\Delta B = \Delta B_{homo} + \Delta B_{inhomo}. \tag{3}$$

The first contribution, ΔB_{homo}, arises from the intrinsic damping that is caused by a combined effect of exchange interaction and spin-orbit coupling (magnetocrystalline anisotropy). The second contribution, ΔB_{inhomo}, originates from broadening due to magnetic inhomogeneities, e.g., the internal static magnetic field. In contrast to ΔB_{inhomo}, the contribution of ΔB_{homo} is proportional to the frequency (25). Superparamagnetic particles exhibit relatively narrow ΔB with $g_{eff} \approx 2$ (26,27). For magnetite samples with a dominant magnetocrystalline anisotropy field, $g_{eff} > 2$ (28), whereas in samples with a prevalent shape anisotropy field caused by the assembly of magnetite in chains, $g_{eff} < 2$ is found (19,24). The asymmetry ratio A is obtained from the shape of the spectra and can be used as a measure for anisotropy. The A-value is ascertained by the ratio of the high-field (ΔB_{high}) and low-field (ΔB_{low}) side of the absorption peak at half-height of the maximum (Fig. 1). Samples with no significant anisotropy exhibit isotropic spectra with $A = 1$. Magnetite at room temperature has a cubic negative magnetocrystalline anisotropy ($K_1 < 0$) and has $A > 1$, i.e., $\Delta B_{low} < \Delta B_{high}$. Positive uniaxial anisotropy with $A < 1$ ($\Delta B_{low} > \Delta B_{high}$) is found for elongated SSD magnetite particles or for magnetite particles aligned along their easy axes forming a dominant shape anisotropy (17,19,24).

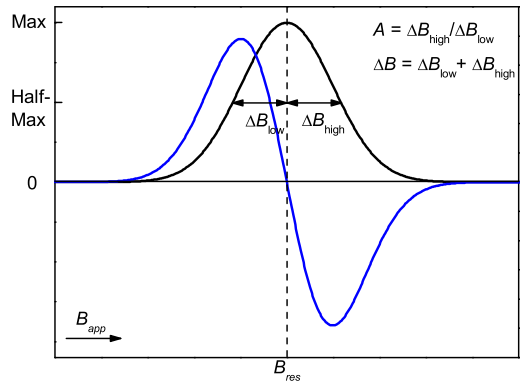

FIGURE 1 Absorption spectrum and first derivative spectrum, with dashed line defining the maximum resonance field (B_{res}) and the zero-crossing. The low-field (ΔB_{low}) and high-field (ΔB_{high}) absorptions at half height of the maximum are indicated; their aspect ratio determines the A-factor, and their sum determines the linewidth ΔB.

FMR analysis

Freeze-dried MTB fixed in an ESR quartz glass tube were used for S- and X-band measurements. The same sample of a growth stage was analyzed for the dual-frequency measurements. The X-band spectra were recorded on a Bruker EMX spectrometer working at a microwave frequency of 9.81 GHz, with a microwave power of 0.06 mW. The applied magnetic field was modulated with a frequency of 100 kHz and a modulation amplitude of 0.1 mT. The S-band FMR spectra were measured on an in-house-built spectrometer controlled by Spec-Man software operating at a microwave frequency of 4.02 GHz and power of 2 mW. The modulation frequency and amplitude of the applied magnetic field were 0.1 mT and 100 kHz, respectively. The spectral parameters A, ΔB and B_{res}, and g_{eff} were obtained from the absorption spectra and its first derivative, respectively.

RESULTS AND DISCUSSION

In the initial stage (T0) of our time-resolved series (i.e., before biomineralization in MTB was triggered by the addition of iron), no magnetite is found in the cells (Figs. 2 *a* and 3 *b*). Because of the high sensitivity of FMR spectroscopy, a weak signal is detected due to ferric cations that cannot be assigned to a specific phase (Fig. 4). After iron addition, the most pronounced production of magnetic particles, as indicated by C_{mag} (21), occurs between T2 and T6 (Fig. 3 *b*).

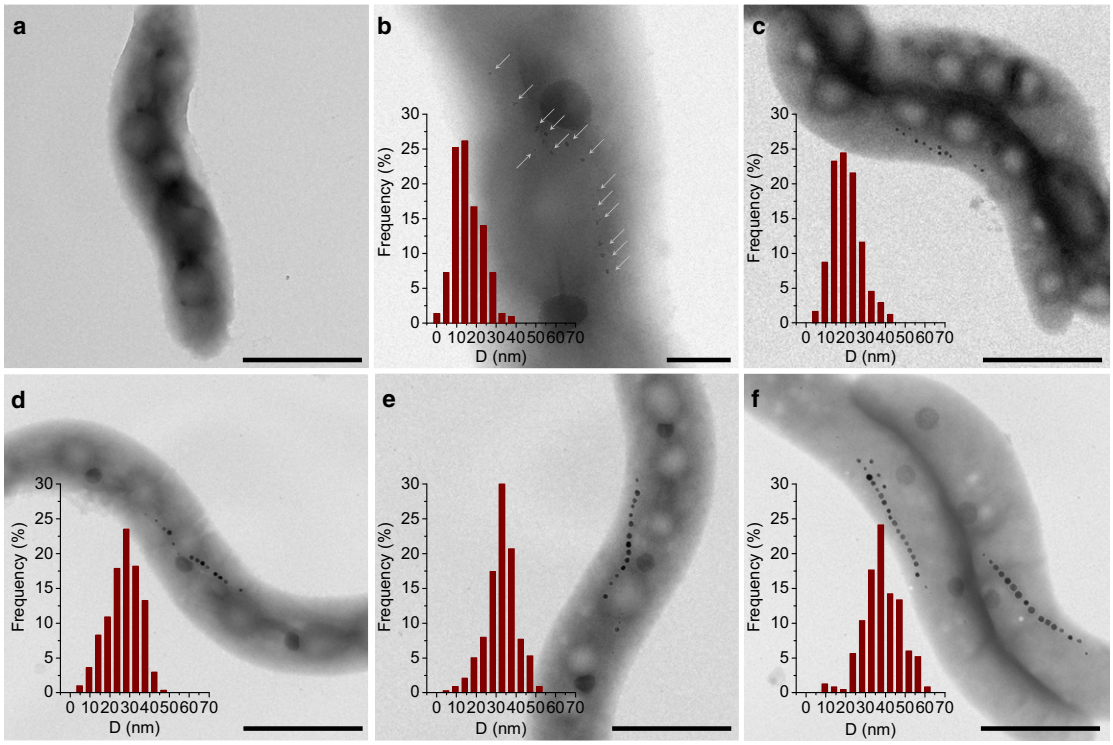

FIGURE 2 TEM images of the MTB and corresponding magnetosome size distributions. (*a*) T0, before iron addition (no magnetite detectable); (*b*) T3, 110 min; (*c*) T6, 280 min; (*d*) T8, 330 min; (*e*) T10, 420 min; and (*f*) T12, 1320 min, after iron addition (scale bars = 1000 nm and 200 nm for T3). Arrows indicate small magnetite particles in T3.

At an early stage of biomineralization (T3), TEM reveals the presence of nearly equidimensional magnetite particles, typical of *Magnetospirilla* strains, with an average dimension of 17.8 ± 7.1 nm (Figs. 2 *b* and 3 *a*, Table 1). At this stage, the FMR spectra recorded at the S- and X-bands exhibit $g_{\text{eff}} = 2.07 \pm 0.2$, symmetric lineshapes (i.e., low- and high-field absorption are nearly identical, leading to $A \approx 1$), and similar ΔB values (Figs. 4 and 5, Table 1). Considering Eq. 3, the marginal frequency dependence indicates a pronounced contribution of ΔB_{inhomo} to ΔB. This behavior, which has also been reported for maghemite nanoparticles with an average size of 23 nm, is probably due to magnetic inhomogeneities in the sample caused by the magnetic state of the magnetosomes (25). The spectral parameters g_{eff} and A, however, suggest that the shape anisotropy of the nearly equidimensional grains is negligible, and no cellular magnetic anisotropy due to interactions is present (17,27,28). This agrees well with theoretical considerations indicating that grain sizes of ~18 nm are far below the threshold of the SPM to SSD state in magnetite of ~30 nm for noninteracting particles (14). Moreover, there is no constraint by a chain assembly that could create magnetostatic interactions to stabilize the thermal fluctuation of the SPM particles. This is supported by TEM images (Fig. 2 *b*) that show spacings between magnetosomes of generally >40 nm, which is too great a distance to allow interactions to build up (29).

At the end of the pronounced magnetosome production (T6), TEM reveals widely spaced particles with sizes indicative of the SPM (<30 nm) and SSD (>30 nm) state. The average size of 22.7 ± 7.3 nm suggests a predominance of SPM particles (Table 1). The S-band spectrum, representing bulk material with millions of magnetosomes, exhibits (for T6 compared with T3) a newly formed shoulder in the low-field range of $B_{\text{app}} < 100$ mT (Fig. 4 *a*). This shoulder points to an increasing number of magnetosomes carrying a remanence magnetization (20). The development of remanence is not FMR-detectable in X-band measurements because the resonance occurs in magnetic fields of >200 mT ($B_{\text{res}} > B_{\text{sat}}$), where the magnetosomes are magnetically saturated, i.e., their spins are fully aligned to the external field (19). In the X-band measurements, however, the change in ΔB between T3 and T6 (Fig. 5) also suggests an enhanced internal static field due to the increase in the number and size of the magnetosomes (26,27,30). Moreover, the similarity of A and g_{eff} obtained from the two spectra (Table 1, Fig. 4 *b*) suggests that at the end of the most pronounced production of particles (Fig. 3 *b*), no functional cellular magnetic dipoles are present.

The TEM images of the T8 and T10 samples exhibit increasing particle dimensions, with average particle sizes of 29.1 ± 8.4 and 34.3 ± 7.6 nm, respectively (Fig. 3 *a*). The larger particle sizes result in the low-field feature in

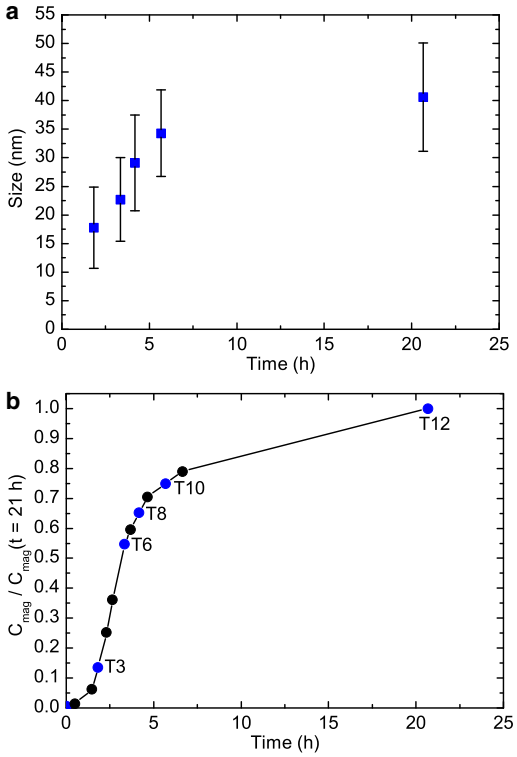

FIGURE 3 (*a*) Evolution of the average magnetosome dimension with time and respective standard deviations. (*b*) The relative magnetic optical density of the cells versus time, with numbered dots for samples analyzed by TEM and FMR spectroscopy.

the S-band, which emerges as a broad peak in sample T8 and a low-field spectral component in sample T10, with $B_{res} = 51$ mT corresponding to $g_{eff} = 5.53$ and clear absorption in the starting field of 5 mT (Fig. 4 *a*). Considering Eq. 2, this absorption near the zero-field can only be explained by a substantial increase in the internal field B_{int}. Such an increase at low field is most likely due to enhanced remanence originating from magnetosomes that are locked together and aligned parallel to the applied field B_{app} (20). Therefore, the development from a shoulder in T6 to a signal with a defined B_{res} in T10 most likely reflects the growth from blocks of a few magnetosomes to larger chains.

The chain arrangement is also documented by the X-band spectra. Sample T8 exhibits a low-field shoulder leading to $A = 0.85$ (Fig. 4 *b*). The decrease in the A-value compared to T6 indicates a slight departure from a nearly symmetric signal due to the generation of shape anisotropy, and therefore provides the first unambiguous spectroscopic evidence for magnetically coupled SSD magnetosomes under conditions with $B_{res} > B_{sat}$. The development of the shoulder to an additional low-field peak in T10 in the X-band spectrum (Fig. 4 *b*) depicts the assembly of magnetosomes into compact chains with pronounced uniaxial magnetic anisotropy ($A = 0.69$). The change in the anisotropy field is also indicated by the jump in ΔB between T8 and T10 in the X-band measurements (Fig. 5, Table 1). In contrast, the jump in the S-band measurements is ambiguous. As mentioned above, the low-field resonance with $g_{eff} = 5.53$ is a selective response of magnetosomes in blocks or chains parallel to B_{app}. The high-field resonance with $g \approx 2$ originates from the other magnetosomes in the bulk sample. The ratio of ΔB of the high-field resonance obtained from the X- and S-band measurements of T10 is 2.15, which is close to the corresponding frequency ratio of 2.44 (Fig. 5). Taking into account Eq. 3, such a ΔB ratio suggests a dominant ΔB_{homo} that is frequency-dependent. Considering the peak-to-peak ΔB over the entire S-band spectrum (low- and high-field resonance), however, the ratio of ΔB is ~1, i.e., both the S-band and the X-band exhibit a jump in ΔB (Figs. 4 *a* and 5). In this case, the ratio indicates a predominant ΔB_{inhomo} contribution to ΔB. Since the two peaks in the X-band spectrum have been interpreted as an anisotropy effect caused by parallel and perpendicular alignments of magnetosome chains to B_{app} (19), it is feasible to postulate that the jump in ΔB in the S-band measurements better represents the bulk properties of the sample (Fig. 5). Hence, ΔB is strongly affected by ΔB_{inhomo}, which most likely arises from an internal static field in the MTB sample.

At T12 (the end of the experiment), TEM reveals narrow-spaced magnetosomes with an average size of 40.6 ± 9.5 nm (Fig. 3 *a*) and a few small (<30 nm) accessory crystals at the chain poles (Fig. 2 *f*). The well-defined low-field spectral component shifts to $B_{res} = 38.6$ mT corresponding to $g_{eff} = 7.33$ in the S-band measurement. This shift points to a stronger B_{int}, which is compelling evidence that in the bulk material as well, most magnetosomes are in an SSD state (Fig. 4 *a*). Moreover, the low asymmetry ratio $A = 0.41$ deduced from the X-band spectrum together with g-values > 2 in the S- and X-bands indicate an even more pronounced magnetic anisotropy of the chains (Fig. 4, Table 1). The FMR spectra and morphology of mature magnetosomes reported in the literature (17–19) are in agreement with those we obtained at the endpoint of our experiments (T12). This shows that our experimental setup is an accurate reflection of the conditions required to form mature and functional magnetosomes in vivo.

Taking the FMR and TEM results together with published genetic information about *M. gryphiswaldense* (7,12), we schematically subdivide the dynamic formation of functional cellular magnetic dipoles in MTB into three steps. In the first step, magnetite nucleation occurs in widely spaced organelles along cytoskeletal filaments. The SPM particles are noninteracting (Fig. 6 *a*). In the second step, the magnetosomes are moved into a closer configuration, most likely by a molecular motor (31), and early-nucleated or faster-growing particles reach the SSD state. The stray field of these particles stabilizes the magnetic dipoles of the remaining and newly formed SPM particles in the adjacencies (Fig. 6 *b*). In this configuration, the SSD particles are considered as magnetic docks that drive the assembly

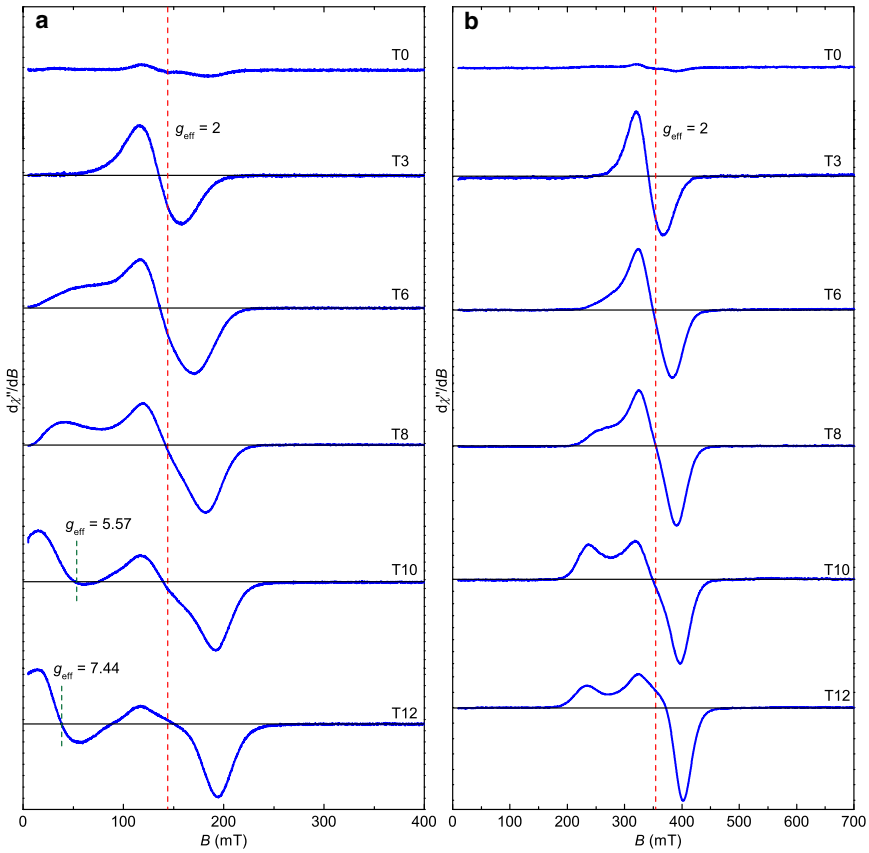

FIGURE 4 First derivative FMR absorption spectra of the time-resolved growth series. (*a*) S-band ($\nu = 4.02$ GHz) spectra of samples representing growth stages before (T0) and after iron addition. The signal intensity of the different growth stages cannot be directly compared because the amount of bacteria per sample varies. The calculated position of $g_{\text{eff}} = 2$ is indicated, and the measured g_{eff}-values of the low-field absorption spectra of T10 and T12 are marked. (*b*) Corresponding X-band spectra with $\nu = 9.81$ GHz.

of closely packed magnetosomes. In the third and final step, long-range magnetic interactions render the chain functional (Fig. 6 *c*). The final adjustment within the chains is obtained by the growth of the vast majority of the magnetosomes above the SPM to SSD threshold ($\approx$30 nm), by fine-tuning of the magnetostatic coupling of magnetosomes optimizing the cellular magnetic dipole, which sustains functionality, i.e., magnetotaxis.

In summary, the assembly of chains is a genetically driven process that utilizes the magnetic properties of the magnetosomes. The magnetic state of the particles plays an essential role in building the magnetic cellular dipoles. Dual-frequency FMR is a powerful tool for investigating the complex processes that result in magnetotaxis. Because magnetic particles or molecules are found in all biological kingdoms (32,33), the combination of biological studies and advanced magnetic spectroscopy techniques can yield new insights into the effects of Earth's magnetic field, as well as fields caused by electromagnetic radiation from technological sources, on living organisms.

TABLE 1 Grain sizes of the magnetosomes (from TEM images) and spectral parameters obtained from X-band measurements, where $B_{\text{res}} > B_{\text{sat}}$

Sample	Grain size [nm]	B_{res} [mT]	g_{eff}	ΔB [mT]	A
T0	-	-	-	-	-
T3	17.8 ± 7.1	341.7	2.05	46.9	1.09
T6	22.7 ± 7.3	349.9	2.01	60.5	1.03
T8	29.1 ± 8.4	354.6	1.98	82.2	0.85
T10	34.3 ± 7.6	349.2	2.01	160.1	0.69
T12	40.6 ± 9.5	371.8	1.89	167.4	0.41

We thank Bill Lowrie and Peter Fratzl for reviewing the manuscript and Håkon Fischer for critical comments on the FMR data.

This project was supported by the Max Planck Society and ETH Zürich.

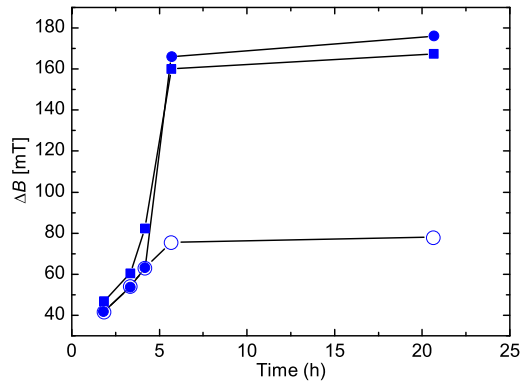

FIGURE 5 Linewidth ΔB obtained during the growth experiment from X-band measurements (*squares*) and from S-band measurements considering the entire spectrum (*solid circles*) and the high-field resonance only (*open circles*).

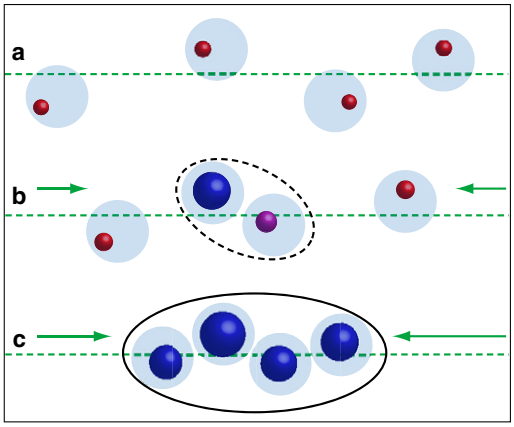

FIGURE 6 Schematic sequence of cellular magnetic dipole formation. SPM magnetite particles (*red*) are nucleated in widely spaced organelles (*light blue*). (*a*) The green arrows indicate the biologically driven movements of the magnetosomes along the cytoskeletal filament (*dashed line*). (*b*) The SSD magnetite (*blue dot*) and its magnetic interaction (*dashed-lined ellipse*) act as a magnetic dock to stabilize SPM particle (*purple dot*). (*c*) The spacing and size of the magnetite are optimized, and the closely spaced magnetite particles separated only by the magnetosome membrane generate a robust cellular magnetic dipole (*solid-lined ellipse*).

REFERENCES

1. Faivre, D., and D. Schüler. 2008. Magnetotactic bacteria and magnetosomes. *Chem. Rev.* 108:4875–4898.
2. Devouard, B., M. Posfai, …, P. R. Buseck. 1998. Magnetite from magnetotactic bacteria: size distributions and twinning. *Am. Mineral.* 83:1387–1398.
3. Bazylinski, D. A. 1995. Structure and function of the bacterial magnetosomes. *ASM News.* 61:337–343.
4. Dunin-Borkowski, R. E., M. R. McCartney, …, P. R. Buseck. 1998. Magnetic microstructure of magnetotactic bacteria by electron holography. *Science.* 282:1868–1870.
5. Simmons, S. L., D. A. Bazylinski, and K. J. Edwards. 2006. South-seeking magnetotactic bacteria in the northern hemisphere. *Science.* 311:371–374.
6. Komeili, A., Z. Li, …, G. J. Jensen. 2006. Magnetosomes are cell membrane invaginations organized by the actin-like protein MamK. *Science.* 311:242–245.
7. Scheffel, A., M. Gruska, …, D. Schüler. 2006. An acidic protein aligns magnetosomes along a filamentous structure in magnetotactic bacteria. *Nature.* 440:110–114.
8. Scheffel, A., A. Gärdes, …, D. Schüler. 2008. The major magnetosome proteins MamGFDC are not essential for magnetite biomineralization in *Magnetospirillum gryphiswaldense* but regulate the size of magnetosome crystals. *J. Bacteriol.* 190:377–386.
9. Ding, Y., J. Li, …, J. Li. 2010. Deletion of the *ftsZ*-like gene results in the production of superparamagnetic magnetite magnetosomes in *Magnetospirillum gryphiswaldense*. *J. Bacteriol.* 192:1097–1105.
10. Carvallo, C., S. Hickey, …, N. Menguy. 2009. Formation of magnetite in *Magnetospirillum gryphiswaldense* studied with FORC diagram. *Earth Planets Space.* 61:143–150.
11. Li, J., Y. Pan, …, W. Lin. 2009. Magnetite magnetosome and fragmental chain formation of *Magnetospirillum magneticum* ABM-1: transmission electron microscopy and magnetic observation. *Geophys. J. Int.* 177:33–42.
12. Faivre, D., L. H. Böttger, B. F. Matzanke, and D. Schüler. 2007. Intracellular magnetite biomineralization in bacteria proceeds by a distinct pathway involving membrane-bound ferritin and iron(II) species. *Angew. Chem. Int. Ed.* 46:8495–8499.
13. Dunlop, D. J., and Ö. Özdemir. 1997. Rock Magnetism: Fundamentals and Frontiers. Cambridge University Press, New York/London.
14. Dormann, J. L., D. Fiorani, and E. Tronc. 1997. Magnetic relaxation in fine-particle systems. *Adv. Chem. Phys.* 98:283–494.
15. Newell, A. J. 2009. Transition to superparamagnetism in chains of magnetosome crystals. *Geochem. Geophys. Geosyst.* 10:Q11Z08. 10.1029/2009GC002538.
16. Faivre, D., N. Menguy, …, D. Schüler. 2008. Environmental parameters affect the physical properties of fast-growing magnetosomes. *Am. Mineral.* 93:463–469.
17. Weiss, B. P., S. S. Kim, …, A. Komeili. 2004. Ferromagnetic resonance and low-temperature magnetic test for biogenic magnetite. *Earth Planet. Sci. Lett.* 224:73–89.
18. Kopp, R. E., C. Z. Nash, …, J. L. Kirschvink. 2006. Ferromagnetic resonance spectroscopy for assessment of magnetic anisotropy and magnetostatic interactions: a case study of mutant magnetotactic bacteria. *J. Geophys. Res.* 111:B12S25. 10.1029/2006JB004529.
19. Fischer, H., G. Mastrogiacomo, …, A. U. Gehring. 2008. Ferromagnetic resonance and magnetic characteristics on intact magnetosome chains in *Magnetospirillum gryphiswaldense*. *Earth Planet. Sci. Lett.* 270:200–208.
20. Mastrogiacomo, G., H. Fischer, …, A. U. Gehring. 2010. Ferromagnetic resonance spectroscopic response of magnetite chains in a biological matrix. *J. Magn. Magn. Mater.* 332:661–663.
21. Schüler, D., R. Uhl, and E. Bäuerlein. 1995. A simple light scattering method to assay magnetism in *Magnetospirillum gryphiswaldense*. *FEMS Microbiol. Lett.* 132:139–145.
22. Wertz, J. E., and J. R. Bolton. 1986. Electron Spin Resonance: Elementary Theory and Practical Applications. Chapman & Hall, New York/London.
23. Vonsovskii, S. V. 1966. Ferromagnetic Resonance. Pergamon Press, Oxford, UK.
24. Kopp, R. E., B. P. Weiss, …, J. L. Kirschvink. 2006. Chains, clumps, and strings: magnetofossil taphonomy with ferromagnetic resonance spectroscopy. *Earth Planet. Sci. Lett.* 247:10–25.
25. Youssef, J. B., and C. Brosseau. 2006. Magnetization damping in two-component metal oxide micropowder and nanopowder compacts by broadband ferromagnetic resonance measurements. *Phys. Rev. B.* 74:214413.
26. Sharma, V. K., and F. Waldner. 1977. Superparamagnetic and ferrimagnetic resonance of ultrafine Fe_3O_4 particles in ferrofluids. *J. Appl. Phys.* 48:4298–4302.
27. Gehring, A. U., R. Karthein, and A. Reller. 1990. Activated state in the lepidocrocite structure during thermal treatment. *Naturwissenschaften.* 77:177–179.
28. Bickford, L. R. 1950. Ferromagnetic resonance absorption in magnetite single crystals. *Phys. Rev.* 78:449–457.
29. Muxworthy, A. R., and W. Williams. 2009. Critical superparamagnetic/single-domain grain sizes in interacting magnetite particles: implications for magnetosome crystals. *J. R. Soc. Interface.* 6:1207–1212.
30. Yulikov, M. M., and P. A. Purtov. 2005. FMR study of superparamagnetic Ni particles with weak and strong anisotropy. *Appl. Magn. Reson.* 29:231–249.
31. Schüler, D. 2008. Genetics and cell biology of magnetosome formation in magnetotactic bacteria. *FEMS Microbiol. Rev.* 32:654–672.
32. Kirschvink, J. L., A. Kobayashi-Kirschvink, and B. J. Woodford. 1992. Magnetite biomineralization in the human brain. *Proc. Natl. Acad. Sci. USA.* 89:7683–7687.
33. Walker, M. M., C. E. Diebel, …, C. R. Green. 1997. Structure and function of the vertebrate magnetic sense. *Nature.* 390:371–376.